J. Fluid Mech. (2005), *vol.* 525, *pp.* 309–332.
DOI: 10.1017/S0022112004002691 Printed in the United Kingdom

Shipping of water on a two-dimensional structure

By M. GRECO[1], O. M. FALTINSEN[2] AND M. LANDRINI[1]†

[1]INSEAN, The Italian Ship Model Basin, Via di Vallerano 139, 00128 Roma, Italy

[2]Centre for Ships and Ocean Structures, NTNU, Norway

(Received 17 November 2003 and in revised form 25 August 2004)

The problem of water shipping is studied by assuming two-dimensional flow conditions and using both experimental and numerical tools. Experimentally, the water on deck for a fixed barge-shaped structure has been analysed. Video images of the water-shipping events were recorded, wave elevation in the wave flume and pressure on a vertical superstructure along the 'ship' deck have been measured. Numerically, a boundary element method for unsteady nonlinear free-surface flows was developed and used for the analysis of water-on-deck phenomena. A comprehensive comparison between experimental and numerical data gave satisfactory agreement globally. The synergic experimental–numerical analysis highlights the main flow features during the water shipping and details of the water impact with the deck structures are discussed. In the model tests, the water on deck started as a plunging wave hitting the deck and entrapping air. This could be relevant for deck safety, but appears to be less important for the global evolution of the water along the deck and the later liquid interaction with the superstructure. The green-water loads on the vertical wall showed a two-peak behaviour typical of wave impacts.

1. Introduction

Water on deck represents a danger for several types of vessel. In rough sea conditions, large masses of water can invade the ship deck and develop in a complicated manner, hitting obstacles on their way. The damage caused by the 'green water' depends both on the vessel characteristics and on the operational conditions at the water-shipping occurrence. As possible consequences, the water flow onto the deck can damage the deck structures, influence the ship dynamics, reduce the passenger comfort, hinder on-board operations or result in the ship capsizing. Despite its relevance for a wide range of ship types (small and large vessels, operating with or without forward speed) this phenomenon is still not completely understood. The research effort in this field is increasing to cover such lack of knowledge and to clarify and quantify the links between water-on-deck occurrence and severity with the main sea and ship parameters.

In severe sea conditions, both vessels with forward motion and ships usually operating in moored conditions, such as the Floating Production Storage and Offloading units (in short FPSO), try to orient themselves against the incoming waves to limit the induced ship motions as much as possible.

The main stages associated with the water shipping can be listed as: water run-up along the ship bow, evolution onto the ship deck, impact with the deck and with

† M. Landrini died on 26 June 2003.

superstructures. However, the water-on-deck features cannot be described through one phenomenological scheme only. In his experimental studies on water-on-deck events caused by head incoming waves on an FPSO model, Buchner (1995) observed a clear similarity between the water invading the ship deck and the flow originated by the breaking of a dam. Model tests by MARINTEK (2000) with an FPSO ship in head sea conditions confirmed Buchner's observations and showed that the dam-breaking type is the most common, but not the only possible water-on-deck scenario. When very steep, almost breaking, waves reach the vessel, the water shipping can occur in the form of a large-scale plunging wave hitting the deck or the superstructures directly. These two types of water shipping can be interpreted as the configurations delimiting the range of possible scenarios.

Present research activity concentrates on bow water-on-deck phenomena in head sea conditions for ships without forward motion. This is relevant for instance for the FPSOs mentioned above. Concerning the FPSO bow-deck wetnesses, although the flow of water along the deck is obviously three-dimensional with water entering the vessel both from the fore bow and laterally (cf. Buchner 1995), two-dimensional investigations can give valuable information since such ships usually have a blunt bow without flare. Three-dimensional experiments by Barcellona *et al.* (2003) showed that, in head-sea waves, the water front velocity along the ship centreline is not particularly affected by the bow shape as long as the bow is sufficiently blunt and without flare. This suggests that the tongue of water along the deck is approximately two-dimensional near the ship centreline. The model tests also documented that the water starts to invade the deck from the fore bow and the resulting flow near the centreline is likely to be the first to impact against the deck house and to cause dangerous water–structure interactions. In this context, a two-dimensional investigation is useful in order to understand the different stages of the water-on-deck events better and to highlight mechanisms which may be less clear when three-dimensional effects are considered.

Here, the water shipping is investigated through a dedicated two-dimensional experimental activity. The features of the phenomenon are described in detail and loads and possible consequences on deck structures are discussed. The analysis is supported by theoretical and numerical tools. A broad variety of numerical methods exists, with related advantages and shortcomings. We developed a boundary element method (BEM) for unsteady nonlinear free-surface flows solving the Laplace equation for the velocity potential. This has been a well-established method for describing plunging breakers for more than twenty years. However, applying the method to green-water loading requires that flow separation from the bow front is accounted for when the water enters the deck. The BEM represents the most accurate and efficient solver as long as potential flow theory is applicable, and proved its qualities in the analysis of many of the physical aspects connected with the water shipping. Obviously, the BEM is not able to capture all the water-shipping features. During water-on-deck events, breaking of the air–water interface can occur, leading to free-surface fragmentation and vorticity generation. They cannot be handled by a BEM and require the use of a field method combined with a suitable technique to describe the evolution of the air–water interface.

In the following sections, the experimental set-up is presented, results of repeatability analysis are given and main error sources involved are quantified and/or indicated. The BEM features are outlined briefly and related novelties to handle water-shipping phenomena are described. Experiments and numerics are then used to investigate the water-on-deck features.

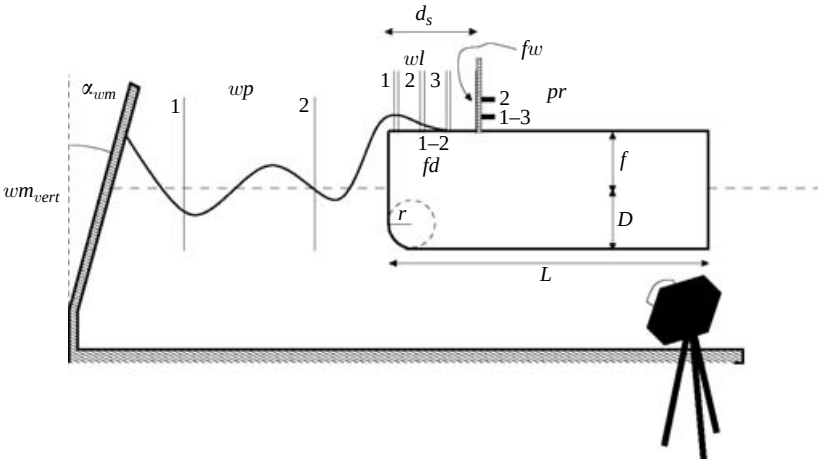

FIGURE 1. Water-on-deck at the bow of a two-dimensional ship. Sketch of the experimental set-up, main involved parameters and sensors used. Side view.

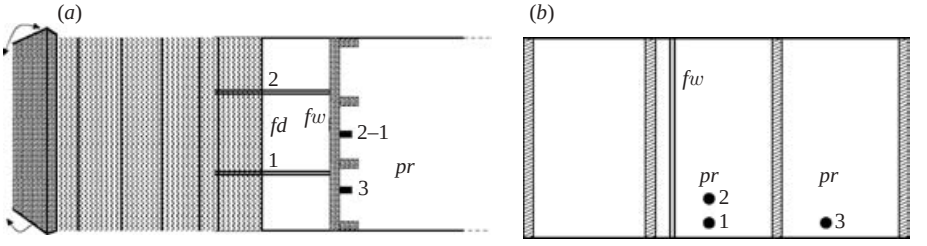

FIGURE 2. Water-on-deck at the bow of a two-dimensional ship. Sketch of the experimental set-up and of the sensors used. (*a*) Top and (*b*) front views.

2. Experimental set-up

2.1. *Equipment*

Two-dimensional water-on-deck model tests have been performed in a narrow wave flume. The flume is 13.5 m long, 1.035 m deep and 0.6 m wide. The sides are 19 mm thick plate glass made to permit flow visualization during tests. Incoming waves were generated by a flap wavemaker hinged at 0.1 m from the bottom. A parabolic beach at the opposite end of the flume reduced the wave reflection. The wavemaker is equipped with a control system constructed by Edinburgh Designs. This is based on monitoring hydrodynamic forces acting on the flap.

A simplified two-dimensional ship model has been used in the tests, characterized by a transparent nearly barge-shaped body with draft $D = 0.198$ m, length $L = 1.5$ m, freeboard $f = 0.05$ m (cf. sketch in figure 1). This means $L/D \simeq 7.6$ and $f/D \simeq 0.253$. The model is made of Plexiglas. The front part of the transparent model has been placed at $\simeq$5.54 m from the vertical wavemaker position (wm_{vert}), while the aft part is about 6.46 m from the opposite side of the flume. The bottom corner at the bow has a radius of curvature $r = 0.08$ m to avoid vortex shedding directly affecting the water shipping on the deck. Finally, the model was restrained from motion in all the tests we performed. Side, top and lateral views of the experimental set-up together with the definition of main geometric parameters are given by figures 1 and 2. Tests have been performed both without and with a vertical wall on the deck, located at $d_s = 0.2275$ m

($d_s/D \simeq 1.15$) from the bow. The vertical wall is transparent and made of Plexiglas. It is rectangularly shaped, ~0.60 m large, 0.30 m high and 0.012 m thick. There are four equi-spaced vertical stiffeners on the back of the wall (see figure 2*b*). A simplified analysis showed a very small highest natural dry-period (about 0.00011 s) for the resulting structure modelled as an equivalent beam. Although not conservative, this estimate suggests that the experiments are not affected by elastic oscillations of the wall owing to water impact.

The flap motion was controlled to generate regular incoming waves. The wavelength range studied is [1.5, 2.5] m, therefore $\lambda/D = [7.6, 12.6]$. Wave heights were selected within the interval [0.08, 0.16] m, and the resulting steepness H/λ varied within [0.04, 0.08]. A linear ramp function of 2 s was used to smooth the initial and final transient motion of the flap, and the total number of oscillations forced in each test was generally about four wave periods. Therefore, the resulting incident waves were far from being regular, both because of the use of the ramp function and, more relevantly, because of the high modulation occurring at the leading crest of a regular wave train. This has to be kept in mind because in the present study we focus on the first water-on-deck event determined, in our case, by the interaction of the bow with a highly non-uniform wave train. The instrumentation used consisted of:

(i) Two capacitive wave probes (with 3 mm diameter) located along the flume: wp_1 at 0.8 m from wm_{vert} (see figure 1) and wp_2 at 0.104 m from the bow.

(ii) Three capacitive wave probes spaced 0.075 m from each other and placed on top of the deck. When the superstructure is not used, the wl_1 centre is at the bow. When the wall is introduced, wl_3 centre is at 0.0405 m from the vertical wall.

(iii) Two capacitive wave probes along the deck (fd_1, fd_2).

(iv) One capacitive wave probe along the vertical superstructure (fw).

(v) Three piezoelectric pressure gauges (diameter of 3 mm) along the vertical superstructure: pr_1 and pr_3 at 12 mm from the deck and horizontally spaced 15 cm from each other, pr_2 at 32 mm from the deck.

(vi) One digital video camera with a standard 25 Hz sampling frequency.

Wave probes on the ship model were characterized by two thin metallic ribbons 5 mm wide glued with a separation distance of 5 mm, and finally calibrated *in situ*. These sensors were used to evaluate the water level along the deck (wl_1, wl_2, wl_3), and to measure the wavefront propagation along the deck (fd_1, fd_2) and during the water run-up along the vertical superstructure (fw). The sampling rate of the measured data was generally 100 Hz.

2.2. *Reliability and repeatability of the measurements*

Repeatability of the tests has been checked. The measurements of the wave elevation time histories by wp_1 and wp_2 are in good agreement, though some tests show a certain deviation from the mean. This is mostly true at the beginning of the time evolution, when the sensitivity and dependence on the initial wave conditions in the flume are the largest. The repeatability for the water-level evolution along the deck (probes wl_1, wl_2 and wl_3) appears acceptable though less good in this case. An important reason is the formation of a cavity of air at the beginning of water on deck. In this context, important factors are represented by the highly transient behaviour of the cavity and by the sensitivity of the sensors to the rate of change of the wetted length along the two strips of each sensor. The propagation of the wave front along the deck (sensors fd_1 and fd_2) shows a satisfactory repeatability in the experiments. In the later stages of the first water on deck, the wetted length measured

decreases, reaching a minimum†. After that, it increases owing to the starting of the next event, which follows a similar evolution cycle. The comparison between the results obtained with sensors fd_1 and fd_2 confirms the two-dimensionality of the flow. In particular, the probes attain non-zero values at the same time instant, and the curves fit quite well until the end of the first water on deck. Differences are observed during the following stages. However, as observed, in this phase the reliability of the measurements is questionable, and the difference is not related to three-dimensional effects, which are negligible according to the analysis of video images‡.

The repeatability for the evolution of the water run-up along the vertical wall, when introduced on the model deck, is quite good until the maximum is approached. Then the measurements vary noticeably, recording different velocities of the rising water and a variation of about 4% in the maximum run-up. The video images show that the flow becomes unstable and three-dimensional during the water rise-up. This explains differences in the results.

The pressure measurements along the wall (sensors pr_1, pr_2 and pr_3) appear similar, but not perfectly repeatable. This is due to both the three-dimensional effects occurring during the water run-up along the wall and to the sensitivity of the measured pressure to the specific flow and environmental conditions. The latter represents a key factor for the reliability of the pressure measurements. The differences between the pressure evolutions at pr_1 and pr_3 are of the same order as those between results recorded at the same gauge during different test runs. This confirms the important role played by the pressure sensitivity to the physical conditions, but it does not exclude the influence of three-dimensional effects. However, these start to matter when the water front, rising along the wall, is far from the pressure sensors and, at least at the beginning, remain localized in the front region. Cross-checks of variables measured on the model were also performed to guarantee their reliability.

Since, in the present experiments, the first water on deck is studied, the time scale of interest was sufficiently small to maintain small the error associated with the seiching oscillations in the tank. More details about the main error sources involved in the experiments can be found in Greco (2001).

3. Numerical solution

Numerically, the water-on-deck problem is solved by using a boundary element method (BEM) for unsteady nonlinear free-surface flows solving the Laplace equation for the velocity potential. Since this is a well-known solver, here only the main features of the present implementation are outlined. Details of the method used can be found in Greco, Landrini & Faltinsen (2004).

An integral representation in terms of source and dipole distributions is used for the velocity potential φ, consistently with Green's second identity. The unsteady problem is solved through the mixed Eulerian Lagrangian scheme (see Longuet-Higgins & Cokelet 1976; Faltinsen 1977), to follow the evolution of the free surface and of the velocity potential on the free surface. The boundary is divided into

† We could question the fact that a decreasing wetted length is measured, since once the probe has been wetted the signal should remain constant. However, below a certain thickness of the layer of water on the deck, capillary effects drive a contraction of the water in the form of isolated wetted regions, with rather unpredictable extent, which are seen from the probe as a reduction of the wetted length.

‡ When small and thin wetted regions appear, the probes are working in a regime where differences in sensor sensitivity imply significant differences in the output signal.

straight-line elements with linear variation for φ and its normal derivative, and with collocation points at the edges of the elements. At the body-free surface intersection points, continuity of the velocity potential is assumed. When the angle between the free surface and the body becomes small, the jet-like flow is partially cut to avoid numerical errors (cf. Zhao & Faltinsen 1993). The discretization of the free surface is controlled through numerical regridding and the grid refinement is adapted to the evolution of the solution. The time integration is performed through a standard Runge–Kutta fourth-order scheme and a dynamic time stepping is used. The latter was found to be crucial to keep the accuracy under control and to have stable solutions during the development of jet flows, breaking waves and impact phenomena. Unphysical reflection of the outgoing waves is prevented by using a damping layer technique, for the short waves, and a panel stretching, for longer wave components, toward the downstream edge of the computational domain. Invariance of the solution under mesh refinement has been widely checked.

Owing to the presence of a sharp corner at the bow edge, the correct description of the water-on-deck occurrence represents a challenging task, independent of the numerical method. In general, one has to use locally a fine discretization. This can be demanding in the case of field solvers. For the BEM method such an aspect is less crucial. On the other hand, an explicit condition has to be enforced at the deck edge. Present two-dimensional experiments showed that at the beginning of the water shipping, the flow always leaves the bow front tangentially and leads to a plunging wave hitting the ship deck and entrapping an air cavity (see § 4.1). These physical observations suggested the development of the following condition.

3.1. *Water-on-deck occurrence: condition A*

The algorithm of condition A is illustrated in figure 3 and the related steps can be described as follows:

1. At the time instant t when the water reaches the freeboard, the free-surface contact point with the body, P_1, is at the deck edge. Here, an ambiguity exists for the wetted body normal vector. In particular, we have the bow-front normal vector and the ship-deck normal vector. For the free-surface point P_1, the bow-front normal vector represents the wetted body normal vector. Therefore, P_1 will leave tangentially the bow front.

2. At the next time instant, $t + \Delta t$, the free-surface point P_1 is no longer a contact point with the body and a new free-surface element is introduced to connect P_1 to the deck edge. This leads to a new free-surface contact point with the body, P_2, at the deck edge.

3. Also for the free-surface point P_2, the bow-front normal vector is taken as the wetted body normal vector. The normal velocity is assumed known and equal to the bow-front normal velocity, zero in our case. The velocity potential φ is unknown and has to be evaluated from the problem. Once known, φ, the velocity vector in P_2 can be fully calculated and will be tangential to the bow front.

4. Steps 2 and 3 are repeated at any time instant until the end of the simulation.

For the experiments considered, condition A appeared able to capture the plunging event and to give information about the features of the water-deck impact. The flow evolution after the water-deck impact and the related green-water loads on the deck could be handled by coupling the BEM with a suitable local solution (see Greco 2001) and modelling the air in the entrapped cavity, but it has not been implemented in this study. The description of the cavity collapse in bubbles (see § 4.1) represents a challenging task. With the aim of analysing also the later stages of the water shipping,

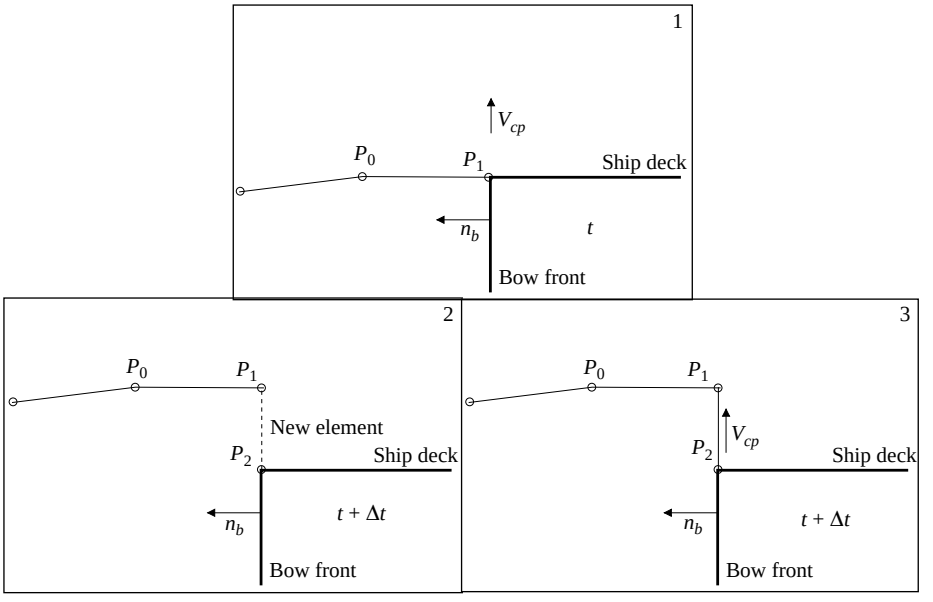

FIGURE 3. Water-on-deck occurrence: algorithm of condition A. 1: the water has reached the freeboard. The free-surface point at the deck edge leaves the bow front tangentially. 2: the water has exceeded the freeboard. A new element is introduced. 3: the free-surface point at the deck edge is forced always to leave the bow front tangentially. Vector $\boldsymbol{n}_b$ indicates the unit vector taken as wetted body normal vector in the evolution of the free-surface contact point with the deck edge. Vector $\boldsymbol{V}_{cp}$ indicates the velocity at the free-surface contact point with the deck edge.

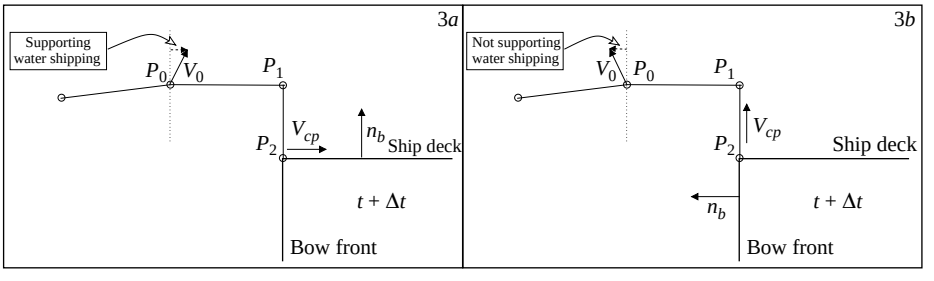

FIGURE 4. Water-on-deck occurrence: step 3 in the algorithm of condition B. 3*a*: water-on-deck occurrence. The free-surface point at the deck edge is forced to move tangentially to the ship deck. 3*b*: no water shipping. The free-surface point at the deck edge is forced to leave the bow front tangentially. Steps 1 and 2 for condition B are the same as those for condition A and are reported in figure 3. The dotted line passing by P_0 is a line parallel to the bow front and the vector $\boldsymbol{V}_0$ represents the velocity in P_0. Vector $\boldsymbol{n}_b$ indicates the unit vector taken as wetted body normal vector in the evolution of the free-surface contact point with the deck edge. Vector $\boldsymbol{V}_{cp}$ indicates the velocity at the free-surface contact point with the deck edge.

we decided to disregard the initial plunging phase and related phenomena and we used the alternative deck-edge condition described next.

3.2. *Water-on-deck occurrence: condition B*

Steps 1 and 2 are identical to those described for condition A. The last step is sketched in figure 4 and can be described as follows:

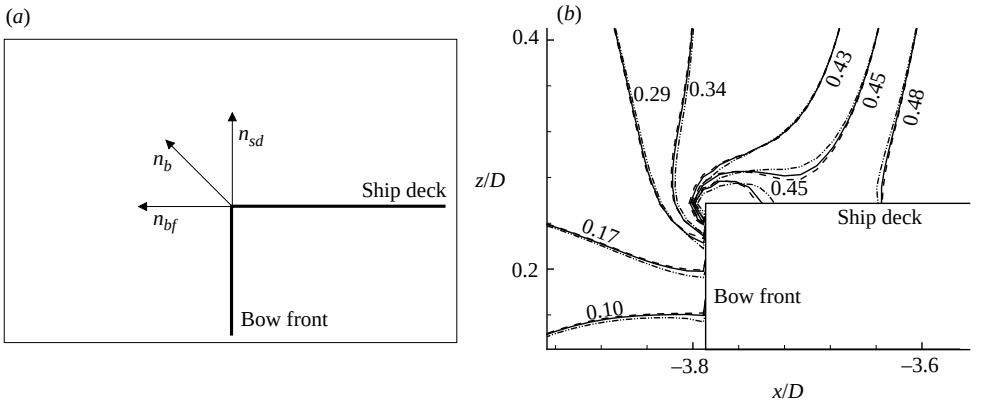

FIGURE 5. Condition B: details of the deck-edge region. (*a*) Sketch for the definition of the normal vector, n_b, used at the deck edge during the water shipping. n_b is arbitrarily taken as the average between the normal to the bow front, n_{bf}, and the normal to the ship deck, n_{sd}. (*b*) Contours of the velocity magnitude at time instant $1.66\sqrt{D/g}$ from the starting of the water on deck. The velocity is made non-dimensional by $\sqrt{gD}$. Three BEM solutions are shown with local refinements $4\Delta x$ (dashed-dot-dot lines), $8\Delta x$ (solid lines) and $16\Delta x$ (dashed lines), respectively. The far-field discretization Δx is the same in the three cases. Nominal regular incoming waves: $\lambda/f = 40$, $H/\lambda = 0.08$.

3. The evolution of the free-surface point P_2 at the deck edge will depend on the local flow velocities: whether or not they support the water-on-deck occurrence. In particular, the velocity of the free-surface point next to P_1, that is P_0, is checked:

3a. If the velocity of P_0, when projected normally to the bow front, gives a vector directed toward the deck, that is, the deck-wetness is supported, then for P_2 the deck normal vector is taken as the wetted body normal vector. Therefore, from this time instant on, P_2 will be forced to move tangentially to the ship deck.

3b. If it gives a vector either zero or directed against the deck, that is the deck-wetness is not supported, then the further evolution is described by enforcing condition A at the deck edge as described above.

Condition B has proved to describe correctly the global water shipping phenomenon and it is useful for investigating the green-water loading on the superstructures. However, we should note that condition B leads in general to a singularity in the flow velocity at the bow edge while condition A does not. In the simulations where condition B is used, once the water shipping has started, at the deck edge the normal to the wetted body is arbitrarily defined as the average between the normal to the bow front and the normal to the ship deck (see figure 5*a*). Using this approach, sufficiently far from the deck edge, the flow features are not influenced by the details around the corner. Further, the numerical results converge even in the close vicinity of the deck edge (cf. figure 5*b*).

An important numerical challenge for both conditions is that, according to the local flow velocities, the elements to be added (see for instance figure 3) could be quite small. To overcome such difficulties, a new element is introduced only when its size becomes comparable to the local discretization near the deck edge.

4. Physical investigations

In the following, the first water-on-deck event is focused on. This implies a transient phenomenon because the incoming waves are far from being regular. As an example,

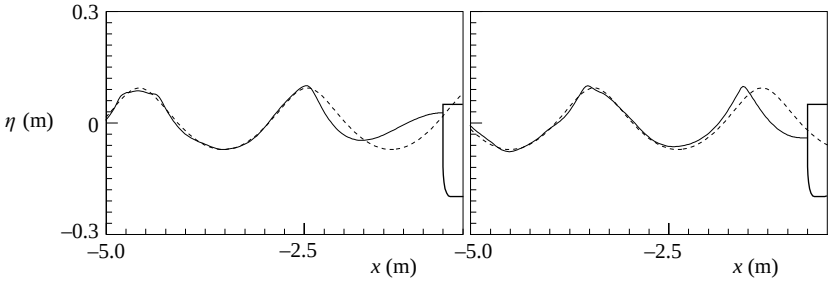

FIGURE 6. Free-surface configurations near the bow before the water-shipping occurrence. BEM solution (solid lines) and permanent-wave solution (dashed lines) by Fenton (1988) are compared. The plots are not in natural scale. Time increases from left to right and corresponds to $t = 7.04$ and 7.66 s, respectively, in the experimental scale. Nominal incoming waves: $\lambda/f = 40$, $H/\lambda = 0.08$.

figure 6 shows the free surface configurations at two time instants obtained by modelling numerically the physical wavemaker and simulating the wave propagation through the BEM. The settings of the control system in the experiment would give steady-state waves 2 m long and with a 0.16 m crest-to-trough height. The corresponding permanent-wave solution, obtained as in Fenton (1988), is compared with the BEM results. Only a rough resemblance between the two solutions can be observed, with the leading wave steeper and shorter than the nominal regular wave. This becomes even more pronounced as the waves approach the ship. Therefore, even though the prescribed wave parameters will be used to identify the wave conditions, we underline the highly transient character of the flow in front of the model.

4.1. *Water shipping: first stages*

4.1.1. *General description*

Figure 7 is representative of the initial stages of the water shipping. The prescribed incoming wavelength and crest-to-trough height are, respectively, $\lambda = 40f$ and $H = 0.08\lambda$. The event is caused by the third wave generated by the wavemaker whose crest is increased by about 24% during the propagation along the flume (see figure 8).

At the beginning of the phenomenon, the fore-part of the deck remains dry, and the shipping of water starts in the form of a rounded jet plunging directly onto the deck. A cavity is formed with air trapped inside. This behaviour has been observed in all the studied test conditions, except for the events characterized by rather small spatial scales. In such circumstances, the surface tension rounded the wave front entering the deck so that the cavity formation was practically prevented (see figure 9 and discussion in § 4.4). In the specific case described here, the jet hits the deck rather close to the bow edge, but cases have also been recorded where the plunging water hits the deck further down the bow. Finally, for some wave conditions, rather blunt impacts were observed along large areas of the deck (see figure 10). In all cases, front-view pictures of the same event (not reported) confirmed the two-dimensionality of the phenomenon, and excluded that the cavity formation is related to any localized three-dimensional instabilities. As a consequence, the initiation of deck-wetting should be characterized by high pressures.

The compressibility of the air entrapped in the cavity could affect the water-induced loads on the deck. In a similar context, comparing experiments and theoretical results, Walkden *et al.* (2001) showed that the air pockets trapped during wave overtopping

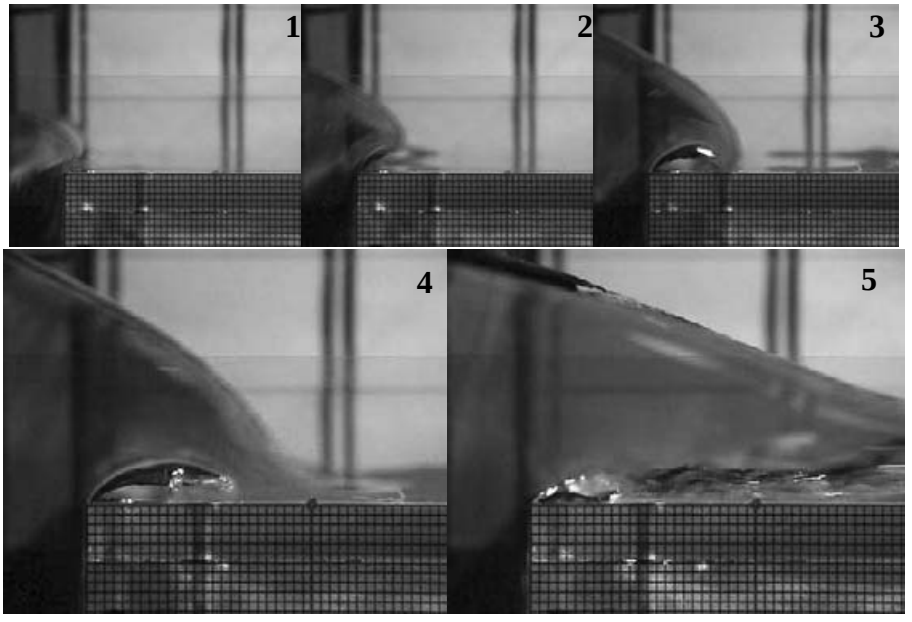

FIGURE 7. Initial stages of water shipping: general features. The phenomenon starts as a plunging wave hitting the deck and entrapping an air cavity. The latter eventually collapses in bubbles. The smallest grid dimension is 2 mm. The snapshots are enumerated as time increases, and the time interval is 0.04 s. Nominal regular waves: $\lambda/f = 40$, $H/\lambda = 0.08$.

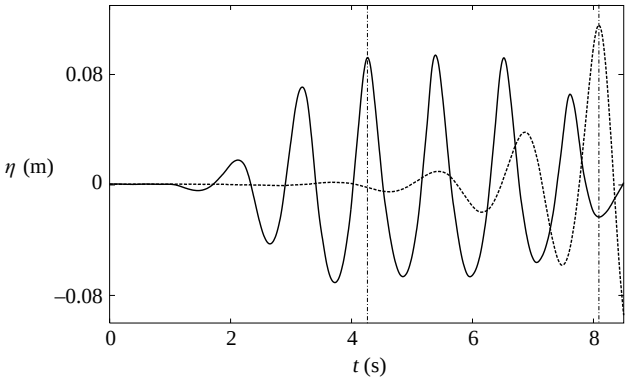

FIGURE 8. Evolution of the wave elevation measured at 0.79 m from the flap (wp_1, solid line) and at 0.104 m from the bow of the model (wp_2, dashed line). The two vertical dash-dotted lines indicate the time instants when the wave responsible of the first water-on-deck phenomenon passes the wave probes. Nominal incoming waves: $\lambda/f = 40$, $H/\lambda = 0.08$.

on caisson breakwaters contribute significantly to the structural pressures. Normally, the deck design does not account for impacts of plunging waves and subsequent air entrainment. In this context, it is relevant to investigate the magnitude and time duration of the green-water loads connected with the initial stages of the water shipping. They should be compared, respectively, to the maximum design load and to the time scale of the highest natural period of the local deck structure. The latter determines to what extent the structure will respond in terms of strains.

FIGURE 9. Initial stages of water shipping: example characterized by rather small spatial scales. The surface tension rounds the water front entering the deck so that the cavity formation is practically prevented. Time increases from left to right with time interval of 0.04 s. Nominal regular waves: $\lambda/f = 40$, $H/\lambda = 0.06$.

FIGURE 10. Initial stages of water shipping: example characterized by rather large spatial scales. The phenomenon starts as a large-scale plunging wave. The impact with the deck appears quite flat and involves a large area of the deck. The thickness of the deck is 11.8 mm. Time increases from left to right with time intervals 0.08 s and 0.04 s, respectively. Nominal regular waves: $\lambda/f = 30$, $H/\lambda = 0.08$.

When air entrainment occurs, it is not clear how to transfer the model scale information to full scale since the Euler number also enters the problem. This governs the compressibility of the entrapped air and is defined as the ratio between the pressure inside the cavity and the dynamic pressure of the surrounding water, respectively counteracting and supporting the cavity closure. Also, owing to the occurrence of an air cavity, the capacity wave probes do not correctly estimate the free-surface height along the deck.

The fluid behaviour described was not detected in the two-dimensional experiments discussed in Cozijn (1995). This may be due to the small time and space scales involved in the initial plunging phase. In the example reported here, the time required by the plunging wave to hit the deck is about 0.13 s, and, at the instant of impact, the entrapped cavity has a length $l_{\mathrm{cav}} \simeq 0.792 f$ and a height $h_{\mathrm{cav}} \simeq 0.198 f$. In Cozijn's model tests, the water shipping caused by regular incoming waves on a bottom-mounted structure was considered. No measurement device was introduced on the 'deck' and the water-on-deck features were investigated by using video images recording the water shipping on a large scale.

The existence of an initial plunging phase has been found in the three-dimensional water-on-deck experiments in Barcellona *et al.* (2003, see § 1). In this case, a video camera was placed inside a fixed ESSO-Osaka model and combined with a mirror system to have bottom views of the bow area during the water shipping. To this aim, a transparent deck was used. The visualizations document a flow evolution similar to our two-dimensional examples.

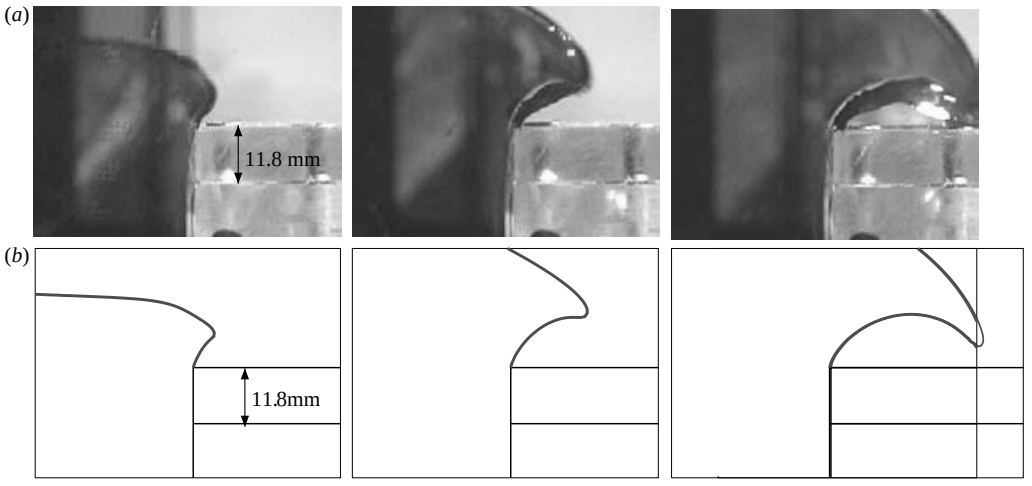

FIGURE 11. Initial stages of water shipping: analysis of the cavity profile. (*a*) Experimental images. (*b*) Numerical free surfaces. Time increases from left to right with an interval of 0.04 s. Nominal regular incoming waves: $\lambda/f = 40$, $H/\lambda = 0.08$.

After the impact of the plunging wave onto the deck, cf. bottom plots in figure 7, two horizontal jets develop. One of these moves backwards, reducing the cavity volume; the other propagates forwards with higher velocity. As time passes, the whole cavity drifts forwards, convected together with the shipped water. The water level above the cavity increases and contributes to its squeezing. These combined actions are responsible, together with surface tension, for fragmentation of the cavity. However, this evolution cannot be documented because of the limited frame rate of the video camera and, in any event, the late evolution of the trapped cavity is three-dimensional.

4.1.2. *Numerics versus experiments*

Figure 11 gives an enlarged view of the plunging phenomenon close to the separation point at the bow. Numerically, the BEM using condition A at the deck edge (see § 3) is able to recover the physical flow evolution. This is confirmed by the satisfactory agreement between the experimental water profiles and the numerical free-surface configurations, also reported in figure 11. In particular, this is true in terms of the time scale of the phenomenon and the cavity dimensions. The differences visible in the sequence can be partially explained by meniscus effects at the glass side of the flume, and by three-dimensional effects in the video images. Moreover, the numerical results do not account for surface tension effects, their role during the initial stages of the experimental water shipping is discussed in § 4.4.

Since, in the experiments, the start of the video camera is not triggered by the wavemaker motion, the triggering between numerics and experimental data has been done heuristically, and it leaves open the possibility of a time lag between experiments and numerical results. This possible error cannot be quantified with the instrumentation used.

From the numerical simulation, the impact occurs at a distance $\simeq 0.792f$ from the bow, after $\Delta t_{wod} \simeq 0.13$ s from the time instant of the freeboard exceedance, $t_{wod} \simeq 7.89$ s.

The essential new contribution made here is not the ability to predict a plunging breaker by using a BEM; this has been documented in the literature over more than

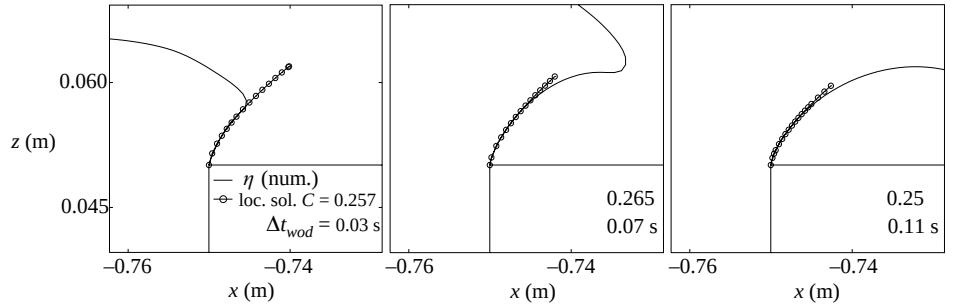

FIGURE 12. Initial stages of water shipping: analysis of the cavity profile. Numerical free surfaces, solid lines, and local solution (4.1), lines with circles, are compared. In the plots, $\Delta t_{wod} = t - t_{wod}$, with $t_{wod} \simeq 7.89$ s the instant when the water exceeds the freeboard. Nominal regular incoming waves: $\lambda/f = 40$, $H/\lambda = 0.08$.

twenty years. The important feature is the treatment of the flow separation from the bow front. Without a proper condition there, we would not have been able to simulate the formation of the air cavity.

4.1.3. *Analysis of the cavity profile*

The satisfactory agreement between experiments and numerics allows us to discuss local features of the phenomenon in full detail.

In figure 12, the free-surface profile close to the separation point at the bow is compared with the local solution

$$z_1 = C(t)\, x_1^{2/3} \tag{4.1}$$

around a fixed separation point, obtained by assuming potential flow theory. This solution follows from satisfying the dynamic and kinematic free-surface conditions and the body-boundary condition and requiring that the flow leaves the bow front tangentially. A brief description of its derivation is given in Appendix A. In (4.1), the origin of the local coordinate system (x_1, z_1) is at the edge of the deck, the x_1-axis is along the deck and the z_1-axis is vertically upwards. The coefficient $C(t)$ is a time-dependent parameter which depends on the complete flow, and therefore cannot be determined by a local flow analysis. For the time instants shown, the local solution with $C \simeq 0.26$, 0.27 and 0.25, respectively, fits the BEM free-surface portion developing from the deck edge quite well.

4.2. *Water shipping: later stages*

4.2.1. *General description*

The sequence of pictures in figure 13 describes the later evolution of the flow field observed in the experiments in a case without superstructures on the deck. The global phenomenon is a dam-breaking-type water on deck (see § 1). The cavity formed at the beginning of the water shipping has collapsed, and bubbles, identifiable as the white region close to the deck, are convected by the main flow propagating rightwards. As the time increases, the role of the gravity becomes important, causing the run-down in front of the bow. Eventually, this leads to the end of the water shipping.

The figure also gives the free-surface configurations obtained by using the BEM method. These, and all the BEM results related to the later stages of water shipping discussed in the following sections, have been obtained by enforcing condition B

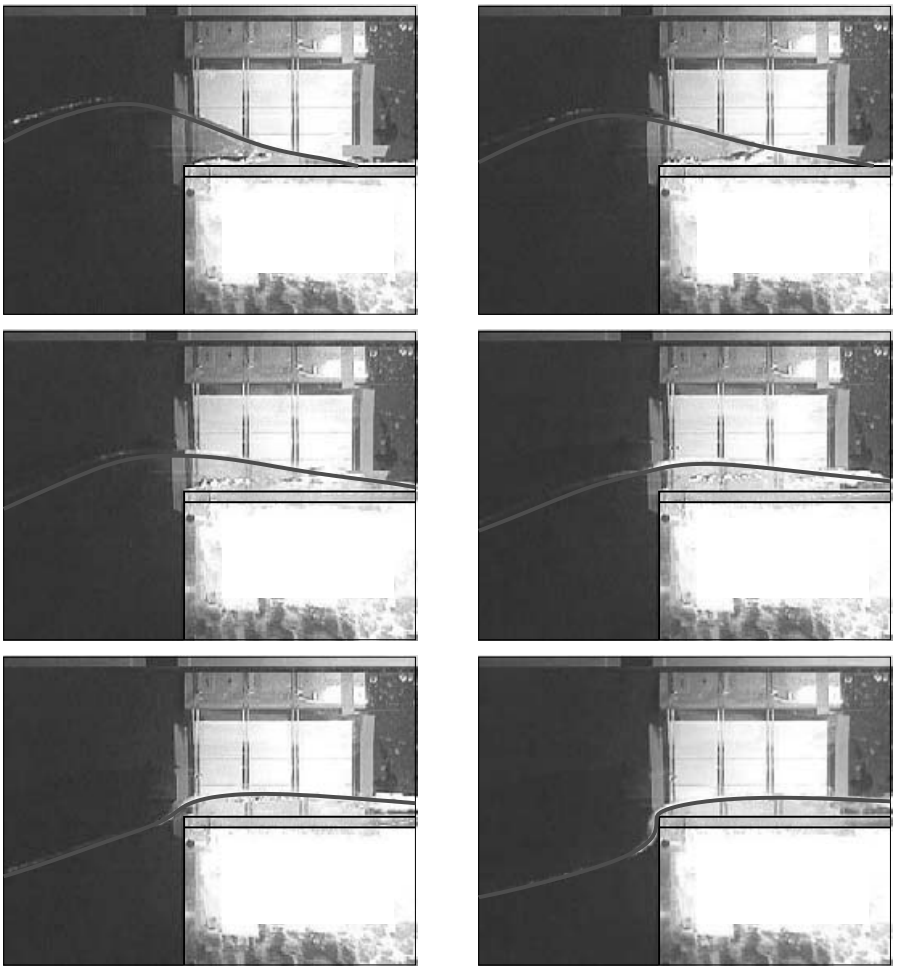

FIGURE 13. Later stages of water shipping on the model without superstructure along the deck. The phenomenon appears as a dam-breaking-type water on deck (see § 1) and the bubbles created by the collapse of the initial cavity are identified by the white region in the water. Numerical free surfaces (solid lines) are superimposed to the experimental video images. The numerics do not model the initial plunging phase. The thickness of the deck is 11.8 mm. Time increases from left to right and from top to bottom with an interval of 0.04 s. In the numerics, the time instants are $\Delta t_{wod} = t - t_{wod} = 0.26, 0.30, 0.34, 0.38, 0.42$ and 0.46 s, with $t_{wod} \simeq 7.89$ s the instant of water-on-deck starting. Nominal regular incoming waves: $\lambda/f = 40$, $H/\lambda = 0.08$.

at the deck edge, that is, the initial plunging phase observed experimentally is not modelled in the numerics. Further surface tension effects are not accounted for. Apparently, though the details of the initial stages of water shipping are neglected, the numerical water profiles agree well with the experimental ones, with the exception of the water front region where the numerical method predicts a higher propagation velocity. The difference between experimental and numerical propagation velocities can be estimated by using measured (sensors fd_1 and fd_2 in § 2) and predicted wavefront evolutions along the deck and remains smaller than 12%. The comparison suggests that the gross flow evolution along the deck is not significantly affected by the phenomena connected with the initial plunging.

FIGURE 14. Evolution of the flow field near the bow edge during the later phases of water shipping. Bubbles are visible, partially convected along the deck and partially involved in the water run-down in front of the bow. To help interpretation of the images, the water profiles have been marked with white curves. The thickness of the deck is 11.8 mm. The time increases from left to right with a time interval of 0.04 s. Nominal regular incoming waves: $\lambda/f = 40$, $H/\lambda = 0.08$.

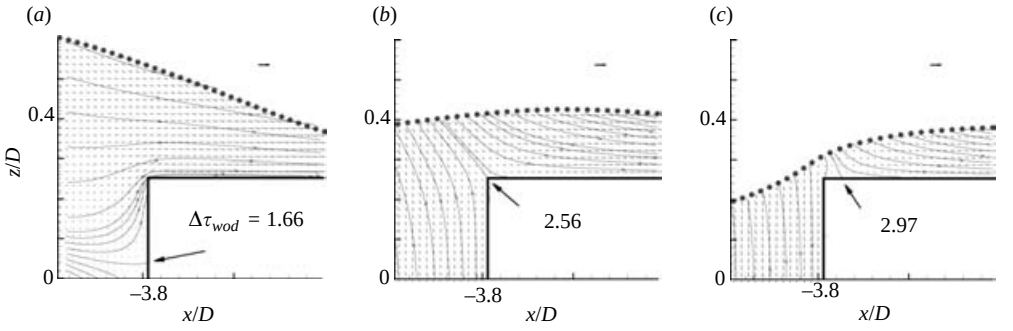

FIGURE 15. Numerical velocity field near the edge of the deck during water shipping. The reference vector has a length equal to $\sqrt{gD}$. The solid lines represent the streamlines, the arrow indicates the location of stagnation point. Nominal regular incoming waves: $\lambda/f = 40$, $H/\lambda = 0.08$.

4.2.2. *Vortex shedding at the edge of the deck*

Natrium flourisenium powder, mixed with Dutch syrup, was used as fluorescent material to detect a possible vortex-shedding in the initial stage of the phenomenon. The resulting mixture was placed in the upper-front portion of the bow. During the tests, the running-up water slowly dissolves the syrup and the fluorescent material is convected with the fluid wetting the deck. For flow past blunt bodies, Skomedal (1985) documented that this procedure is suitable for vortex-shedding visualizations. Here, by using this method, we have not detected any clearly defined vortical structure during the initial stages of the water shipping. Later on, after the air entrapment and when the cavity starts to move forward along the deck, the gravity has already organized the run-down of the fluid in front of the model. This prevents the shedding of vortices strong enough to be detected by the used method. This is qualitatively shown in figure 14, where an enlarged view of the flow around the bow is given for the later stages of the water shipping. By tracking the motion of the entrapped air bubbles visible in the water, we can see that the bubbles above the deck are convected rightwards, while those in front of the bow move downwards.

4.2.3. *Velocity field in the bow area*

Figure 15 gives the numerical velocity field near the edge of the deck during the water shipping. When most of the water enters the ship deck (figure 15*a*),

FIGURE 16. First stages of water impact with a vertical wall at 0.2275 m from the bow: enlarged view. The incoming water front can be approximated as a half-wedge. The impact causes a jet rising along the structure. Time increases from left to right with time interval of 0.04 s. Nominal regular incoming waves: $\lambda/f = 40$, $H/\lambda = 0.08$.

FIGURE 17. First stages of water impact with a vertical wall at 0.2275 m from the bow: global view. Numerical free surfaces (solid lines) are superimposed to the experimental video images. In the numerics, the initial plunging phase has not been modelled. Time increases from left to right with a time interval of 0.04 s. In the numerics, the time instants are $\Delta t_{wod} = t - t_{wod} = 0.273$, 0.313 and 0.353 s, with $t_{wod} \simeq 7.89$ s the instant of water-on-deck starting.

the stagnation point is located somewhere along the front of the bow. This would suggest the occurrence of a vortex shedding from the sharp corner. However, the initial plunging phase has not been modelled in the simulation, while in reality the formation of the initial cavity, discussed in § 4.1, prevents the vortex-shedding phenomenon. Later on, once the gravity has forced the water run-down at the bow, the stagnation point moves to the deck edge (figure 15*b*), dividing the flow in two parts, as discussed in § 4.2.2. Then, it proceeds further along the deck during the final phase of the water shipping (figure 15*c*).

4.3. *Impact with a vertical wall*

4.3.1. *Water evolution*

Figure 16 shows an enlarged view of the water impact occurring when a vertical wall is introduced along the deck, at 0.2275 m from the bow. Nominal incoming waves are $\lambda = 40f$ long and $H = 0.08\lambda$ high. The water front approaching the structure is rounded near its intersection with the deck. This could be due to surface tension and/or boundary-layer effects (see Greco 2001). Neglecting these very localized features, the water front can be approximated as a half-wedge with small interior angle. At the beginning of the water–wall interaction, only a small amount of the fluid, sharply deviated upwards by the obstacle, is affected by the impact. The water flow is deflected to form a vertical jet, and some spray occurs. Figure 17 shows the impact phenomenon on a smaller scale. From this view, only the leading portion of the water hitting the wall can be approximated locally by a half-wedge. The rest of the incoming

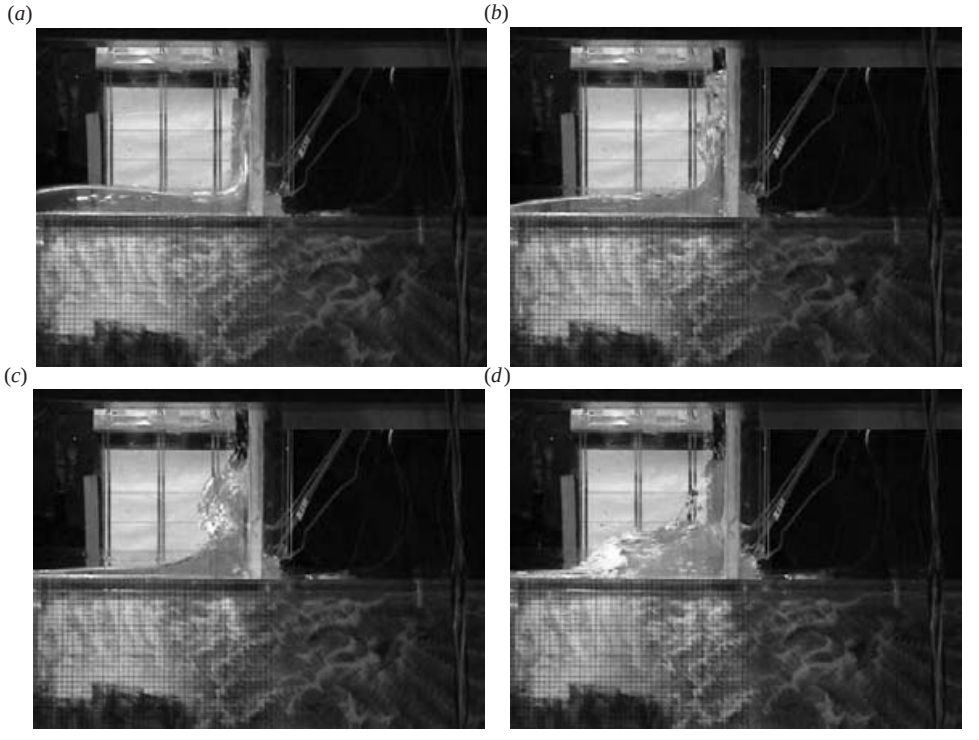

FIGURE 18. Later stages of the water–wall interaction. Top: final stages of the water run-up along the wall. Bottom: water overturning and breaking during the water run-down phase. Time increases from left to right and from top to bottom with a time interval of 0.08 s. Nominal regular incoming waves: $\lambda/f = 40$, $H/\lambda = 0.08$.

water has a more general shape. The BEM free-surface profiles are superimposed to the experimental images and fit the water profiles well. In the numerics, the initial plunging phase has not been modelled, therefore the water–superstructure interaction is also not substantially affected by the details of the bow flow.

As time increases, the layer of water impacting on the wall becomes thicker (see on figure 18*a*) while the flow causing the structure to rise is slowed down by the gravity action. At this stage, three-dimensional instabilities occur, as discussed in § 2. After that, the free surface at the water front is no longer smooth (see figure 18*b*). Eventually, the fluid motion is converted into a water run-down by the gravity. This thickens the layer of liquid near the vertical wall and causes the formation of a backward plunging wave hitting the underlying water and entrapping air (see figure 18*c*, *d*). Vorticity is then generated as a consequence of the water–water impact and the BEM based on solving the Laplace equation for the velocity potential is not appropriate anymore.

4.3.2. *Pressure along the vertical wall*

The pressure evolution on the wall, measured at 0.012 m and 0.032 m above the deck (see figure 2), is reported in figure 19. As discussed in § 2, the experimental curves are similar, but not perfectly repeatable. All the pressure records show the presence of two main peaks. Between these two maxima there are oscillations, especially at the lower sensor location, with an average period of about 0.075 s. The reasons for the oscillations are not clear. The period is very large compared with the highest natural

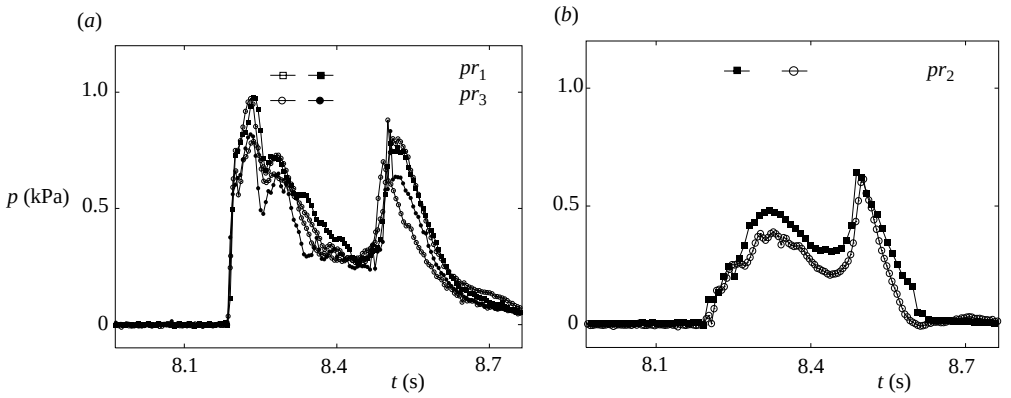

FIGURE 19. Pressure evolution on the vertical wall measured at (*a*) 0.012 m and (*b*) 0.032 m above the deck. Two test results are shown for each pressure gauge used in the tests (see figure 2 for the sensor definitions). Nominal regular incoming waves: $\lambda/f = 40$, $H/\lambda = 0.08$.

period of the vertical wall (see § 2) so the oscillations are not explained by elastic vibrations of the superstructure. Care has been taken to ensure that the sensors were aligned to the wall surface. In the case of a non-perfect alignment, a bubble, either associated with the spray created during the water rise along the wall or convected from the bow area by the main flow, could be entrapped and oscillate above the sensor surface. In our case, the related natural period would be much smaller than 0.075 s owing to the small gauge diameter (see Faltinsen 2005). Further, we observed whether there were bubbles in the fluid and estimated qualitatively the frequencies of dynamic pressure oscillations due to the bubbles. However, this phenomenon could not give a plausible explanation. The cause of the oscillatory behaviour is still under investigation.

The first peak in the pressure evolution occurs at the beginning of the water run-up along the wall and is connected with the initial impact of the liquid with the structure. As a result, it is higher at the lowest location and almost disappears at the upper one. At these early stages of the water–wall interaction, the fluid acceleration dominates over the gravity. This is confirmed by the pressure results at the lowest location reported in figure 20. Here, the experiments are compared with the BEM calculations for the same water-on-deck phenomenon, and with the zero-gravity simulation of a liquid half-wedge hitting a wall at 90° (see figure 20*b*). The latter represents a simplification of the water–wall impact and is based on the assumption that the phenomenon is governed by the shape and the velocity of the incoming waterfront, and the gravity does not play any role. The applicability of approximate solutions is very important, particularly at the design stage. In the present case, the simplified problem correctly describes the initial stages of the impact, as discussed later. The zero-gravity solution has been obtained numerically by using the similarity solution in Zhang, Yue & Tanizawa (1996) for the free-surface data and taking the impact velocity, V, and the half-wedge angle, β, as predicted by the BEM. In the BEM simulation, the initial plunging phase is not modelled. The comparison shows that the initial rise of the pressure is captured well by the zero-gravity results. Therefore, gravity can be neglected in predicting the maximum pressure associated with the initial impact. This is reported in figure 20(*c*) as a function of the impact angle. From the results, if β is small enough (less than about 40°) V dominates the impact phenomenon. This was the case for all the water-on-deck events studied in

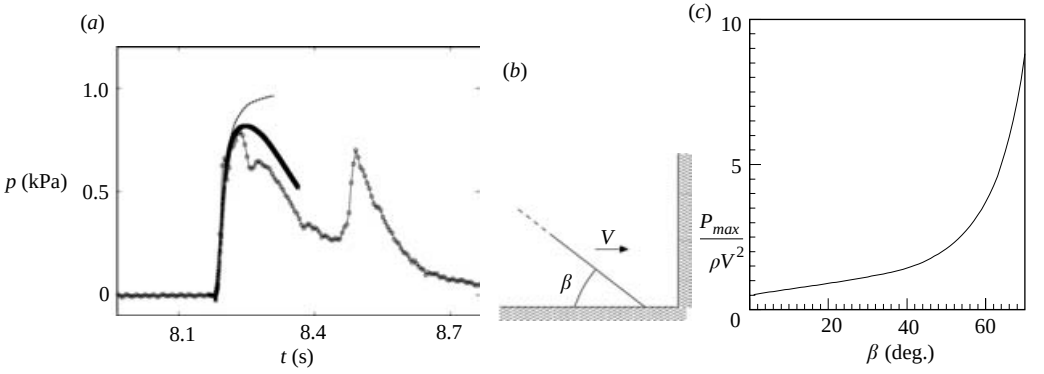

FIGURE 20. Left: pressure evolution on the vertical wall measured at 0.012 m above the deck. Experimental data (line with symbols, only one measurement is shown for plot clarity), BEM results (thick solid line) and zero-gravity solution for the liquid half-wedge impact problem (dashed line). The latter has been obtained numerically by using the similarity solution by Zhang *et al.* (1996) for the free surface conditions and taking the impact velocity V and half-wedge angle β (see center sketch in the figure) as predicted by the BEM. In the BEM simulation the initial plunging phase has not been modeled. Nominal regular incoming waves: $\lambda/f = 40$, $H/\lambda = 0.08$. Center: sketch of the problem of a fluid half-wedge impacting a flat wall at 90 degrees. Right: maximum pressure on the wall obtained by solving the zero-gravity problem sketched in the center plot.

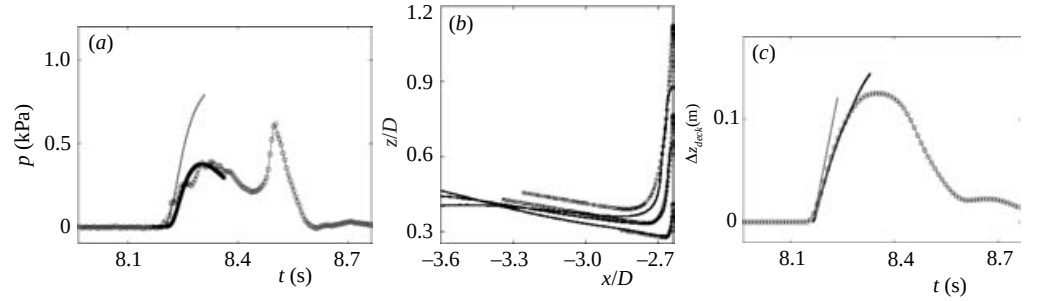

FIGURE 21. (*a*) Pressure evolution on the vertical wall measured at 0.032 m above the deck. (*b*) Free surface configurations given by the BEM (solid lines) and by the similarity solution (lines with circles) in Zhang *et al.* (1996) at the time instants 0.605, 0.685 and $0.764\sqrt{f/g}$ after the start of water shipping, $t_{wod} \simeq 7.89$ s. (*c*) Water-run up along the vertical wall. The results in (*a*) and (*c*) are experimental data (lines with symbols, only one measurement is shown for plot clarity), with-gravity solution by the BEM (thick solid lines) and zero-gravity solution (dashed lines) obtained numerically using the similarity solution by Zhang *et al.* (1996) for the free surface conditions and taking the impact velocity V and half-wedge angle β as predicted by the BEM. In the BEM simulation the initial plunging phase has not been modelled. Nominal regular incoming waves: $\lambda/f = 40$, $H/\lambda = 0.08$.

the experiments, that is, the water reached the structure roughly as a liquid half-wedge with small interior angle. In circumstances like these, the prediction of the flow velocities along the deck is very important to guide the design of deck superstructures. The zero-gravity solution predicts higher maximum pressure than the experiments and BEM at the lower sensor location. The overestimate becomes even larger at the upper location (see figure 21*a*). More than being due to gravity effects, such disagreement is due to the fact that the incoming water profile resembles the half-wedge only in the waterfront region, as previously discussed. This is confirmed by the comparison

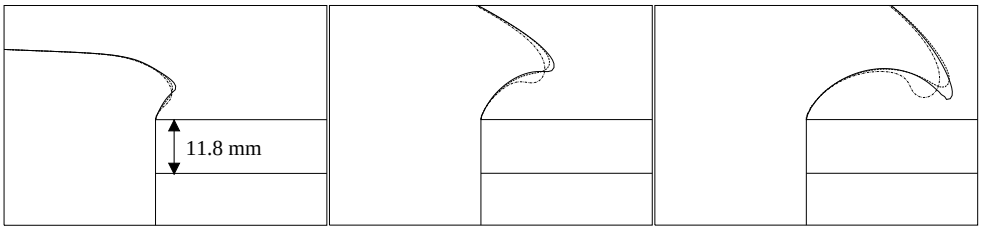

FIGURE 22. Two-dimensional water-on-deck experiments. Initial stages of the water shipping due to nominal regular waves with $\lambda/f = 40$ and $H/\lambda = 0.08$. Numerical free surfaces with surface tension at model scale, dashed-dot lines, and at full scale, dashed lines ($D = 18$ m), and results without surface tension, solid lines. The time increases from left to right with time interval of 0.04 s. Corresponding experimental images are given in figure 11(*a*).

between the free-surface configurations predicted by the BEM and similarity solution during the water run-up along the structure (see figure 21*b*). Only at the early stages of the water–wall interaction does the BEM free-surface fit locally the liquid half-wedge hitting the structure. Later on, the incoming water is characterized by a thinner layer. As a result, the similarity solution also predicts a faster run-up with respect to the experiments and BEM simulation (see figure 21*c*).

After the first pressure peak, the water–wall interaction reduces and the experimental pressure decreases to a minimum value (see figure 19). Then, it starts to rise again and a second peak occurs during the final stages of water shipping, with similar peak values at the two sensors along the vertical wall. Cross-checking the pressure measurements with the run-up data and with the water-on-deck visualizations, it appeared that the second pressure rise occurs during the water run-down phase.

The observed two-peak pressure behaviour is consistent, for instance, with the pressure time history measured by Walkden and described in Peregrine (2003) within the study of breaking waves impacting against vertical breakwaters. Peregrine refers to the curve as the typical impact profile measured in the tests in cases of violent wave impacts and names it a 'church roof' profile owing to the double-peak behaviour. The first peak is explained by the initial water–wall impact. The second peak is much lower and is explained by the pressures required to decelerate the falling water. In the present experiments, the two peaks are of the same order of magnitude. This is because the initial water-wall impact is not particularly violent and the mass of falling water is relatively large compared with the layer of water on the deck.

4.4. *Surface tension effects in the experiments*

Although surface tension effects do not play any substantial role at full-scale, they could be relevant during model tests and must be quantified before converting experimental results to full scale. Computations of the effect of surface tension on a rising jet have been provided by Jervis & Peregrine (1996). In our work, their importance during the initial stages of the experimental water shipping is analysed numerically by using the BEM and enforcing condition A at the deck edge (see § 3).

The initial stages of the first water-on-deck due to prescribed incoming waves with $\lambda/f = 40$ and $H/\lambda = 0.08$ are given in figure 22. From the results, at model scale the surface tension rounds the tip of the plunging wave and causes a delay in the flow evolution. In this case, the latter is $\Delta t' \simeq 0.005$ s. To facilitate the comparison, this delay has been avoided, that is the results without surface tension at time t have been compared with those accounting for surface tension at time $t + \Delta t'$. The results with surface tension are closer to the experimental water evolution (cf. figure 11*a*)

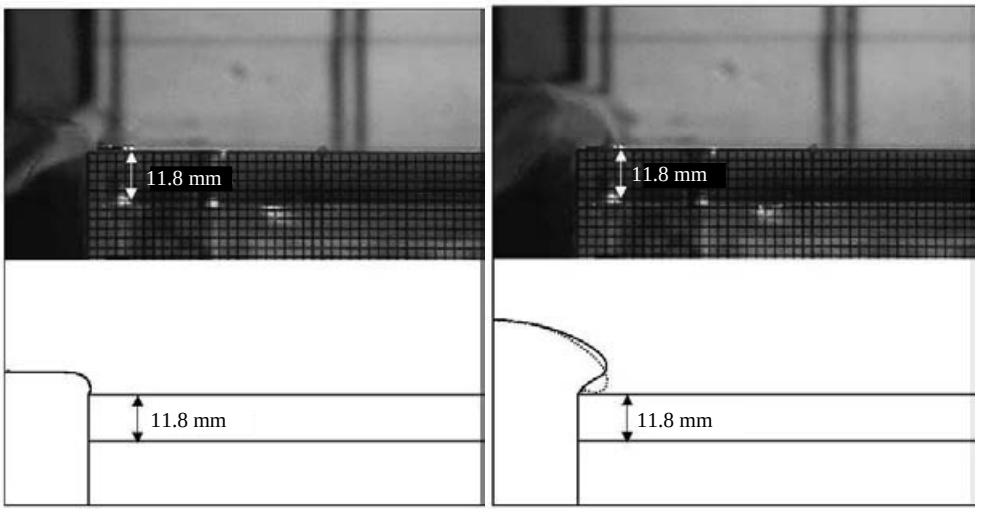

FIGURE 23. Two-dimensional water-on-deck experiments. Initial stages of the water shipping due to nominal regular waves with $\lambda/f = 40$ and $H/\lambda = 0.06$. Top: experiments. The smallest grid dimension is 2 mm. Bottom: numerical free surfaces with (dashed lines, experimental scale) and without (solid lines) surface tension. The time increases from left to right with time interval of 0.04 s.

than the corresponding results free from surface tension (also reported in figure 11*b*). This confirms the influence of surface tension on the tests. On the other hand, except for the local area at the front tip, the full scale (by using a draft $D = 18$ m as for a FPSO ship) free surfaces are not affected by surface tension (see figure 22). As a consequence of the surface tension effects, the wave plunging onto the experimental deck is blunter than at full scale and will impact closer to the bow. In the extreme cases of very small spatial scales, the rounding of the plunging wave owing to the surface tension practically prevents cavity formation. This is shown in figure 23 for the prescribed incoming waves with $\lambda/f = 40$ and $H/\lambda = 0.06$.

5. Conclusions

The bow deck wetness phenomenon for a stationary ship restrained from oscillating, with blunt bow, and in regular head waves, has been idealized and reduced to a two-dimensional wave–body interaction problem.

The problem has been investigated through a dedicated experimental activity. The analysis of model test results was supported by theoretical and numerical tools. Numerically, a BEM for nonlinear unsteady free-surface flows has been used and specialized for the analysis of water-on-deck phenomena. Details on how the flow separation from the bow front is incorporated are presented in the paper. The experiments have revealed details of the flow when the water is initially shipped onto the deck. Within a small time scale, the shipping of water starts in the form of a plunging breaker, hitting the deck close to the bow. This causes the formation of a cavity eventually broken into bubbles. The water–deck impact and the air compressibility in the cavity could be relevant for the deck safety. In this context, local investigations of the green-water loads in the bow area are important. The influence of surface tension on the evolution of the initial plunging has been discussed by using the experimental images and BEM simulations with and without surface-tension

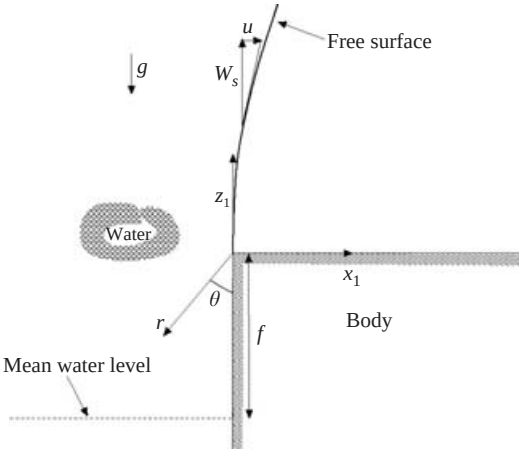

FIGURE 24. Sketch of the problem and symbols used.

effects. From the results, the surface tension played a role in the model tests, rounding the plunging wave and causing a water–deck impact closer to the bow. According to the physical observations, the later flow evolution on the deck is not characterized by relevant vortex shedding near the bow. The initial plunging wave hitting the deck is a localized phenomenon. After this rapid phase, the water shipping develops in the form of a dam-breaking-type water on deck with the gross flow evolution not affected by the initial plunging phase. The impact of shipped water against a deck house has also been analysed. At the early stages of the impact, gravity does not matter and the impact flow can be approximated by a zero-gravity similarity solution. In this case, a fluid half-wedge hitting a straight wall at 90°. The combined use of the zero-gravity similarity solution and the flow visualizations during the water shipping confirm the velocity of the impacting water as an important parameter for the design of the superstructures. As time goes on, the similarity solution overpredicts the pressure along the wall, mainly because the water reaching the structure does not resemble the half-wedge globally. In addition to the pressure peak caused by the initial water impact with the superstructure, the experiments showed a second peak of the same order of magnitude in the evolution of the pressure along the wall. This peak appears in the later stages and is related to the falling water. Therefore, these late events are also important.

This work was partially supported by the Centre for Ships and Ocean Structures, NTNU, Trondheim, within the 'Green Water Events and Related Structural Loads' project, and partially done within the framework of the 'Programma di Ricerca sulla Sicurezza' funded by *Ministero Infrastrutture e Trasporti*. The basis of this work is Greco's PhD thesis at NTNU.

Appendix. Local solution around a fixed separation point

Here, the derivation of the local solution (4.1) is briefly outlined.

A local analytical solution in the vicinity of a fixed separation point is investigated (see figure 24). A Cartesian (x_1, z_1) and a polar (r, θ) coordinate system, with common origin at the separation point, are considered and the flow is assumed two-dimensional in the (x_1, z_1)-plane. The local solution of the velocity potential φ, that is for small

values of r, is written as

$$\varphi = a(t) + W_s(t)\, z_1 + \underbrace{A\, r^n \cos n\theta}_{\phi}, \tag{A 1}$$

where $a(t)$, $W_s(t)$, A and n are unknowns to be determined. In particular, $a(t)$ and $W_s(t)$ represent, respectively, the velocity potential and the tangential velocity to the wetted body at the separation point (see figure 24). Equation (A 1) satisfies the body boundary condition since $r^{-1}\partial\varphi/\partial\theta$ is zero at $\theta = 0$, implying that there is no flow through the body boundary. We must satisfy the dynamic free-surface condition. This requires that the pressure is atmospheric at the free surface, and using the Bernoulli equation becomes

$$\frac{\partial\varphi}{\partial t} + \frac{1}{2}\rho\,[u^2 + (w + W_s)^2] + \rho\, g\,(z_1 + f) = 0\,. \tag{A 2}$$

Here, f is the vertical distance from the mean water level (see figure 24) and u and w are, respectively, the x_1- and z_1-components of the flow velocity due to the velocity potential ϕ in (A 1). Consistent with the fact that a local solution is required, equation (A 2) is approximated by linearization onto $\theta = \pi$ (or $x_1 = 0$ and $z_1 > 0$). Further, we assume that u and w are small compared with W_s and are of lower order with respect to r, that is, they are $O\,(r^{n-1})$ with $n - 1 < 1$. This implies terms with different orders of magnitude in equation (A 2), that can be ordered as follows

$$\underbrace{\frac{\mathrm{d}a}{\mathrm{d}t} + \frac{1}{2}\rho W_s^2 + \rho g f}_{O(r^0)} + \underbrace{\rho W_s w}_{O(r^{n-1})} + \underbrace{\frac{1}{2}\rho[u^2 + w^2]}_{O\left(r^{2(n-1)}\right)} + \underbrace{\frac{\mathrm{d}W_s}{\mathrm{d}t} z_1 + \rho g z_1}_{O(r)} = 0. \tag{A 3}$$

Here, (A 1) has been used. The lowest-order terms in (A 3) lead to the link

$$\frac{\mathrm{d}a}{\mathrm{d}t} + \tfrac{1}{2}\rho W_s^2 + \rho g f = 0 \tag{A 4}$$

between the unknowns a and W_s. To the next order, we must satisfy

$$\rho W_s w = 0. \tag{A 5}$$

Assuming $W_s \neq 0$, this implies that

$$w|_{\theta=\pi} = n r^{n-1} A \cos n\pi \quad \rightarrow \quad n\pi = \tfrac{1}{2}\pi,\ \tfrac{3}{2}\pi \ldots \tag{A 6}$$

Since r is assumed small, the lowest possible n has to be considered. However, $n = 1/2$ would imply an infinite velocity at $r = 0$, while the flow must leave the body smoothly from the separation point. Therefore, the solution is given by $n = 3/2$, which is consistent with our assumption that $n - 1 < 1$. Equation (A 5) is also satisfied by $A = 0$ which corresponds to water flowing straight upwards, see (A 1). The values of A for all the other solutions, which may be summed because the boundary condition is linearized, are determined by the rest of the flow field.

Considering a quasi-steady approach valid, a first approximation of the free-surface profile can be obtained by noting that it must be a streamline. Then, its slope is given by

$$\frac{\mathrm{d}x_1}{\mathrm{d}z_1} = \frac{u}{W_s + w} \simeq \frac{u}{W_s}, \tag{A 7}$$

where the approximation comes from the orders of magnitude assumed for the velocity components. Substituting in (A 7) the u expression

$$u = \frac{1}{r} A r^{3/2} \frac{\mathrm{d}\cos(3\theta/2)}{\mathrm{d}\theta}|_{\theta=\pi} = \tfrac{3}{2} A r^{1/2} \tag{A 8}$$

and integrating it, we finally obtain

$$x_1 = \underbrace{\frac{A}{W_s}}_{C^{-1}} z_1^{3/2} \quad \rightarrow \quad z_1 = C(t) x_1^{2/3}, \tag{A 9}$$

which is the same as (4.1). To find the values of A, W_s and a we must define the far-field conditions and match them with the local solution.

REFERENCES

Barcellona, M., Landrini, M., Greco, M. & Faltinsen, O. M. 2003 An experimental investigation on bow water shipping. *J. Ship Res.* **47**/**4**, 327–346.

Buchner, B. 1995 On the impact of green water loading on ship and offshore unit design. *Proc. Intl Symp. Practical Design of Ships and Mobile Units, PRADS'95*, *Seoul*, pp. 430–443.

Cozijn, J. L. 1995 *Development of a calculation tool for green water simulation.* MARIN Wageningen/ Delft University of Technology, Delft, The Netherlands.

Faltinsen, O. M. 1977 Numerical solutions of transient nonlinear free-surface motion outside or inside moving bodies. *Proc. of 2nd Intl Conf. Numer. Ship Hydrodynamics, University of California, Berkeley*, pp. 347–357. Extension Publications.

Faltinsen, O. M. 2005 *Hydrodynamics of High-Speed Marine Vehicles.* Cambridge University Press.

Fenton, J. D. 1988 The numerical solution of steady water wave problems. *Comput. Geosci.* **14**, 357–368.

Greco, M. 2001 A two-dimensional study of green-water loading. PhD thesis, Dept of Marine Hydrodynamics, NTNU, Trondheim, Norway.

Greco, M., Landrini, M. & Faltinsen, O. M. 2004 Impact flows and loads on ship-deck structures. *J. Fluid Struct.* **19**, 251–275.

Jervis, M. & Peregrine, D. H. 1996 Overtopping of waves at a wall: a theoretical approach. In ASCE (ed.), *Proc. 25th Intl Conf. on Coastal Engng, vol. 2, Orlando, USA*, pp. 2192–2205.

Longuet-Higgins, M. S. & Cokelet, E. D. 1976 The deformation of steep surface waves on water. I. A numerical method of computation. *Proc. R. Soc. Lond.* A **350**, 1–26.

MARINTEK 2000 *Review No. 1 April.*

Peregrine, D. H. 2003 Water-wave impact on walls. *Annu. Rev. Fluid Mech.* **35**, 23–43.

Skomedal, N. G. 1985 *Application of a vortex tracking method to three-dimensional flow past lifting surfaces and blunt bodies.* PhD thesis, Dept of Marine Technology, NTNU, Trondheim, Norway.

Walkden, M., Wood, D. J., Bruce, T. & Peregrine, D. H. 2001 Impulsive seaward loads induced by wave overtopping on caisson breakwaters. *Coastal Engng* **42**, 257–276.

Zhang, S., Yue, D. K. P. & Tanizawa, K. 1996 Simulation of plunging wave impact on a vertical wall. *J. Fluid Mech.* **327**, 221–254.

Zhao, R. & Faltinsen, O. M. 1993 Water entry of two-dimensional bodies. *J. Fluid Mech.* **243**, 593–612.